

The LLAGN in the centre of the Galaxy

M. Contini

School of Physics and Astronomy, Tel Aviv University, Tel Aviv 69978, Israel

Accepted: Received ; in original form 2010 month day

ABSTRACT

The observations of FIR line and continuum spectra throughout the Galactic centre and in some regions of the disc are analysed in order to determine the physical conditions (densities, shock velocities, radiation parameters, etc.) and the relative abundances of some elements (C, N, and O). The models account for the coupled effect of photoionization and shocks. Consistent model calculations of the line and continuum spectra show that, although the radiation from the stars dominates, an active galactic nucleus (AGN) is clearly present, with a radiation maximum in the Sgr A* region. The flux, similar to that found for low luminosity AGN (LLAGN), is lower by a factor of ~ 100 than that of AGN. Gas densities in the downstream line emission region range between 100 and 2000 cm^{-3} , the shock velocities between 50 and 300 km s^{-1} . Densities of $\sim 5 \times 10^6 \text{ cm}^{-3}$, close to the Sgr A* black hole, lead to self-absorption of free-free radiation in the radio frequency range, while X-ray data are explained by shock velocities of $\sim 3000 \text{ km s}^{-1}$. A magnetic field of $\sim 10^{-4}$ gauss shows relatively small fluctuations throughout the Galactic centre. The dust-to-gas ratios range between 3×10^{-15} and $\leq 10^{-13}$ by number. Lower values are found far from the centre, suggesting that N and O, which are depleted from the gaseous phase, are included into molecules rather than trapped into grains.

Key words: Galaxy:centre–shock waves–radiation mechanisms–ISM:abundances–galaxies:line spectra

1 INTRODUCTION

Acceleration measurements of stellar orbits near the radio source Sgr A* suggest the existence of a supermassive black hole at the Galactic centre (Ghez et al. 2003; Schödel et al. 2003). Recently, Genzel et al (2010) showed from the analysis of more than two dozen orbits and from measurement of the central compact radio source Sgr A*, that this must be a massive black hole (BH) of $\sim 4.4 \times 10^6 M_{\odot}$.

In particular, the BH in the central Sgr A West HII region (Ghez et al. 2005; Eisenhauer et al. 2005) is coincident with the radio source Sgr A* and with a cluster of massive stars. Two other clusters of young massive stars and massive molecular clouds (Schödel et al. 2006) appear near the Galactic Centre (GC), the Arches Cluster and the Quintuplet Cluster located ~ 25 pc away in the plane of the sky. The very massive Arches Cluster (Nagata et al 1995 and Cotera et al. 1996) of young stars heats and ionizes the region of the Arched Filaments. The Quintuplet Cluster ionizes the Sickle and affects the clouds in extended regions including the Bubble.

The Galactic central regions are strongly obscured to UV-optical spectroscopic observations. The morphology of the regions near the GC, recently revealed at radio frequen-

cies, shows a turbulent regime on a large scale (Simpson et al. 2007, fig.1).

The GC contains within only 5 arcmin (12 pc) a massive BH surrounded by a rotating circumnuclear disc of dust and gas, HII regions, massive stellar clusters, two SNRs, and two giant molecular clouds (Amo-Baladrón et al 2011).

The BH is surrounded by gas and dust. The gas is photoionized by a dense stellar population from the central cluster. Other stars are distributed throughout the central region and the disc. Therefore the GC shows a composite nature of AGN and starburst galaxy. Moreover, turbulent dynamical motions (e.g. arc-shaped gas streamers with a minispiral morphology) imply a shock dominated regime.

The GC has been used as a test for many models that attempt to explain the physics of low luminosity AGN (LLAGN) in the last years (e.g. Anderson et al. 2004). In fact, the luminosity of Sgr A* is extremely low, even compared with other LLAGNs.

In AGNs as well as in low-luminosity objects, such as LLAGNs and LINERs (low-ionization nuclear emission regions) starbursts coexist with an active nucleus, affecting the spectra with comparable importance (Contini et al 2002, Contini 1997, 2004a). Modelling the X-ray-IR continuum correlation in a large sample of AGN, Contini et al. (2003)

confirmed that LLAGNs appear in the low-luminosity tail of AGN. This is explained by the relatively low flux from the active nucleus, roughly by two orders of magnitude lower than found in the NLR of Seyfert galaxies (Contini 2004a). Moreover the velocity field is relatively low.

Spitzer observations of IR spectra (Simpson et al 2007 and references therein) near the GC were analyzed by Contini (2009, hereafter Paper I), leading to a detailed picture of gas and dust structures near the GC. The modelling revealed the results of ionization and heating of the gaseous clouds by the young massive stars in the Quintuplet Cluster, the Arches Cluster, etc. The presence of shocks generated by the turbulent regime observed in these regions, definitively explained the NIR spectra. The comparison of line ratios calculated by the models with those observed in the IR was constrained by a sufficiently high number of ions. The models accounted for the coupled effect of photoionization by a black body (BB) flux from the stars and shocks.

The models, which explained the observed IR spectra, were used to calculate the UV and optical lines which cannot be observed because strongly obscured (Contini & Goldman 2010, hereafter Paper II). Comparison with observations of active galaxies (starbursts, AGN, LINERs, LLAGNs, etc) confirmed that the spectra near the GC are similar to those dominated by a BB flux. However, an active nucleus was not excluded. Dust details emerged from the consistent modelling of the spectral energy distribution (SED) of the continuum in the different regions.

The results of Papers I and II show that some line ratios from regions near the GC are similar to those of low luminosity active galaxies, but the gaseous clouds are strongly fragmented by the underlying turbulence (Paper II).

In the very central region of the Galaxy, there is observational evidence for star-formation activity. The star-forming clouds, such as the Sgr B2, Sgr C, Sgr D, and the 50 km s^{-1} clouds in the Sgr A, show that the star-formation activity is high (Yasuda et al 2008).

Far-IR (FIR) spectra were observed in different regions of the GC. Yasuda et al (2008) report on spectroscopic observations with the Long-Wavelength Spectrometer (LWS) on board the Infrared Space Observatory (ISO). Owing to the wide wavelength coverage (43 to $197 \mu\text{m}$) of the ISO/LWS, they could study multiple fine-structure lines at the same time, which were used to determine the physical conditions of the interstellar medium (ISM). Previous ISO observations in the GC were reported by many authors, including H II regions (Rodríguez-Fernández et al. 2004), giant molecular clouds (Lis et al. 2001) and discrete objects near the GC (Cotera et al. 2005; Goicoechea et al. 2004).

Most of these observations focus on local regions, whereas Yasuda et al. observations cover much larger GC regions. The targets of Yasuda et al are not particular regions, such as active H II regions, but typical regions in the GC least contaminated by strong discrete sources. Rodríguez-Fernández et al. (2004) observed similar regions.

Yasuda et al attempted to characterise the difference of general clouds in the GC region from those in the disc, and therefore selected GC as well as disc positions. Rodríguez-Fernández et al. concentrated on the GC region. Unfortunately, the lines observed by Rodríguez-Fernández et al. do not constrain the models.

Goicoechea et al. (2004) too observed the Sgr B2 region

in the FIR fine structure emission lines, [N II], [N III], [O III], [C II], and [O I] and concluded that the local radiation field in the Sgr B2 region is characterized by a hard ionizing continuum typical of an O7 star with a radiation effective temperature T_{eff} of $\sim 36\,000 \text{ K}$. Many of the line intensity fluxes are upper limits, therefore the spectra cannot be used for a detailed modelling (see, however, the next sections).

In this paper we investigate the GC regions and the few disc ones by modelling the ISO/LWS archived data presented by Yasuda et al. (2008), accounting for both the star and the AGN characteristics of the GC. First we will calculate the physical conditions of the emitting gas adopting a BB dominated radiation flux corresponding to $T_{\text{eff}} \sim 36\,000 \text{ K}$. Then, we will examine the AGN calculating the spectra by a power-law (pl) radiation flux with suitable spectral indices.

According to Lis et al (2001) the harsh environment in the GC region (central $\sim 200 \text{ pc}$ of the Milky Way), the region referred to as the central molecular zone, characterized by disruptive tidal forces, high gas pressures (Bally, Stark, & Wilson 1988; Spergel & Blitz 1992), and strong magnetic fields (Morris & Yusef-Zadeh 1989), may suppress gravitational collapse in all but the most massive clouds. Consequently, star formation may be caused primarily by shock compression caused by cloud-cloud collisions,

The Galactic plane just outside the central molecular zone between $l=1.3^\circ$ and 5° contains several localized cloud complexes with unusually large velocities (Bally et al. 2010) of $\sim 100\text{-}200 \text{ km s}^{-1}$ in regions less than 0.5° ($\sim 75 \text{ pc}$) in diameter.

Therefore, we adopt for the calculation of the spectra the code SUMA¹ which simulates the physical conditions of an emitting gaseous nebula under the coupled effect of photoionization from an external source and shocks. Both line and continuum emission from the gas are calculated consistently with dust reprocessed radiation,

The shock velocities, the preshock densities, the ionization parameters, and the relative abundances are calculated phenomenologically. The models are described in Sect. 2, the results regarding the line spectra are presented in Sect. 3. The SED of the continuum is analyzed in Sect. 4.

In particular, after having unveiled the LLAGN in the GC by modelling the line spectra, we will try to reproduce consistently the SED of the Sgr B2 observed continuum and of other LLAGNs (Falcke et al 1998, Anderson et al 2004) in the radio domain. The results are presented in Sect. 4.2.

Finally, an interesting issue concerns the [CII]157.5/FIR ratios, where FIR is the continuum FIR flux. Yasuda et al. claim, on the basis of the low [CII]/FIR ratio in the central region of the Galaxy, that the dominant sources of the FIR luminosity in the GC region are not young OB stars, but K and M giants, implying a low star-formation activity.

The [CII] lines are emitted from the gas, while the continuum FIR represents dust reprocessed radiation rather than bremsstrahlung, depending on the dust-to-gas ratios. Dust reradiation dominates the SED in the FIR range. So in this paper, we will address the [CII]/FIR question in the GC (Sect. 4.3) on the basis of the dust-to-gas ratios.

Discussion and concluding remarks follow in Sect. 5.

¹ <http://wise-obs.tau.ac.il/~marcel/suma/index.htm>

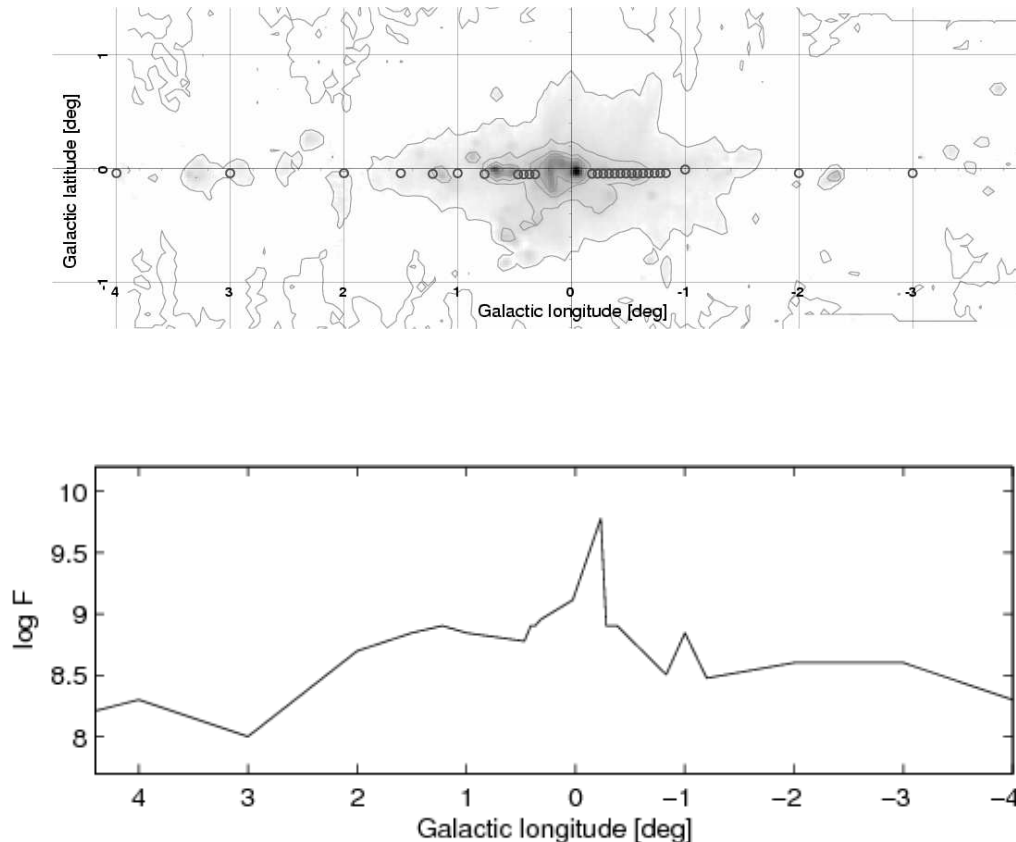


Figure 1. top diagram : ISO/LWS observational points in the Galactic centre region, plotted on the 10 GHz radio continuum map (Handa et al 1987), adapted from Yasuda et al (2008, fig. 1). Bottom diagram : the calculated radiation flux F corresponding to power-law dominated models.

2 THE MODELS

In previous investigations of the physical conditions near the GC (e.g. Simpson 2007) the shocks were invoked to explain the line ratios and the FWHM of line profiles. Moreover an underlying shock generated turbulence was confirmed on the basis of the power spectra of the radial velocities (Paper II).

Therefore, to model the spectra in the GC and in the disc, we will take into account the effects of shock wave hydrodynamics coupled to the photoionization flux from the stars, or to the photoionization power-law flux from AGN.

The spectra observed in each position by Yasuda et al are relatively poor in number of lines. However, the FIR lines presented in each spectrum, are suitable to constrain the model physical parameters. Yet the calculation of the relative abundances requires some general assumptions (see Sect. 3.4). Therefore, we cannot select BB or pl dominated fluxes by the best fit of the spectra, as was done e.g. for the Seyfert galaxy NGC 7130 (Contini et al. 2002).

In the present investigation, we will calculate each spectrum adopting BB and pl dominated models (in two different sets of models), both reproducing as much as possible the line ratios. The weighted sum of the line intensities calculated by the two models will give acceptable results whichever the relative weights adopted.

In this way, our modelling will not provide definitive results in each position, namely if the stars or the active

nucleus dominate the radiation field, but some interesting results will arise from the distribution of the parameters throughout the GC and the few disc positions (Fig. 1).

In particular, the emitting clouds move either towards the radiation source or outwards. Consequently, the flux from the stars (or from the active centre) reaches the shock front edge or the edge opposite to the shock front, respectively. The code SUMA is adapted to both cases. When the cloud recedes from the photoionizing source, the calculations are iterated up to convergency of results. The geometrical thickness of the emitting nebula plays an important role particularly in this case.

We adopt a plane-parallel geometry. The calculations start at the shock front where the gas is compressed and thermalized adiabatically, reaching the maximum temperature in the immediate post-shock region ($T \sim 1.5 \cdot 10^5 / (V_s/100 \text{ km s}^{-1})^2$). T decreases downstream following the cooling rate, which is calculated in each slab downstream. This region is cut into a maximum of 300 plane-parallel slabs with different geometrical widths, which are calculated automatically, in order to follow the temperature gradient.

The input parameters: the shock velocity V_s , the preshock density n_0 , the preshock magnetic field B_0 , define the hydrodynamical field. They are used in the calculations of the Rankine-Hugoniot equations at the shock front and downstream. These equations are combined into the compression equation which is resolved throughout each slab in

order to obtain the density profile downstream. The results of line intensity calculations in each slab depend strongly on the density. A detailed description of model calculations is given in Paper I.

The input parameters that represent the radiation field are : the colour temperature of the stars T_{eff} and the ionization parameter U for black body dominated fluxes, or the power-law flux from the active center F in number of photons $\text{cm}^{-2} \text{s}^{-1} \text{eV}^{-1}$ at the Lyman limit. if the photoionization source is an active nucleus. Both U and F are calculated by radiation transfer throughout the slabs downstream.

The dust-to-gas ratio (d/g) and the abundances of He, C, N, O, Ne, Mg, Si, S, A, Fe relative to H, are also accounted for. They affect the calculation of the cooling rate.

The dust grains are heated radiatively by photoionization and, collisionally, by the shock. The distribution of the grain radii downstream is determined by sputtering, beginning with an initial radius of $1.0 \mu\text{m}$.

The input parameters which lead to the best fit of the line ratios determine the physical conditions in each of the observed positions.

3 LINE SPECTRA

Yasuda et al. (2008) selected 28 observations from the centre and 5 observations from the disc, which are least contaminated by the active H II regions; the observational points in the GC region are shown in Fig. 1. They refer to the region between $-3^\circ \leq l \leq 4^\circ$ as to the GC region; the disc region is outside this area. All the observation points are close to the Galactic plane.

Strong continuum emission and six fine-structure atomic emission lines have been detected. The lines are : [O III] $52 \mu\text{m}$ ($^3\text{P}_2 \rightarrow ^3\text{P}_1$), [O I] $63 \mu\text{m}$ ($^3\text{P}_1 \rightarrow ^3\text{P}_2$), [O III] $88 \mu\text{m}$ ($^3\text{P}_1 \rightarrow ^3\text{P}_0$), [N II] $122 \mu\text{m}$ ($^3\text{P}_2 \rightarrow ^3\text{P}_1$), [O I] $145 \mu\text{m}$ ($^3\text{P}_0 \rightarrow ^3\text{P}_1$), and [C II] $158 \mu\text{m}$ ($^2\text{P}_{3/2} \rightarrow ^2\text{P}_{1/2}$) in most of the GC and in a few disc regions. The intensities of the emission lines were obtained by Gaussian plus linear fitting.

3.1 The line ratios

A reliable information about the physical conditions throughout the GC, is obtained by modelling line *ratios* rather than *absolute fluxes* because they avoid problems of distances, absorption etc..

In this paper we refer to the spectra presented by Yasuda et al (2008) in their table 1. We adopt line ratios to [OI]63 which is a relatively strong line. The observational errors of the data are rather high. Nevertheless, we have tried to reproduce the line ratios as precisely as possible.

Four of the six observed lines imply oxygen ions, therefore the oxygen relative abundance will not seriously affect the choice of the physical parameters. We start by modelling the observed line ratios, in particular [OIII]51.8/[OI], [OIII]88.4/[OI] and [OIII]51.8/[OIII]88.4 by BB and pl dominated models in two different sets of calculations.

We notice that the calculated [OIII]51.8/[OIII]81.4 line ratios depend strongly on the shock velocity. Actually, V_s defines the postshock maximum temperature of the gas, while the [OIII] line ratios should depend mainly on the density

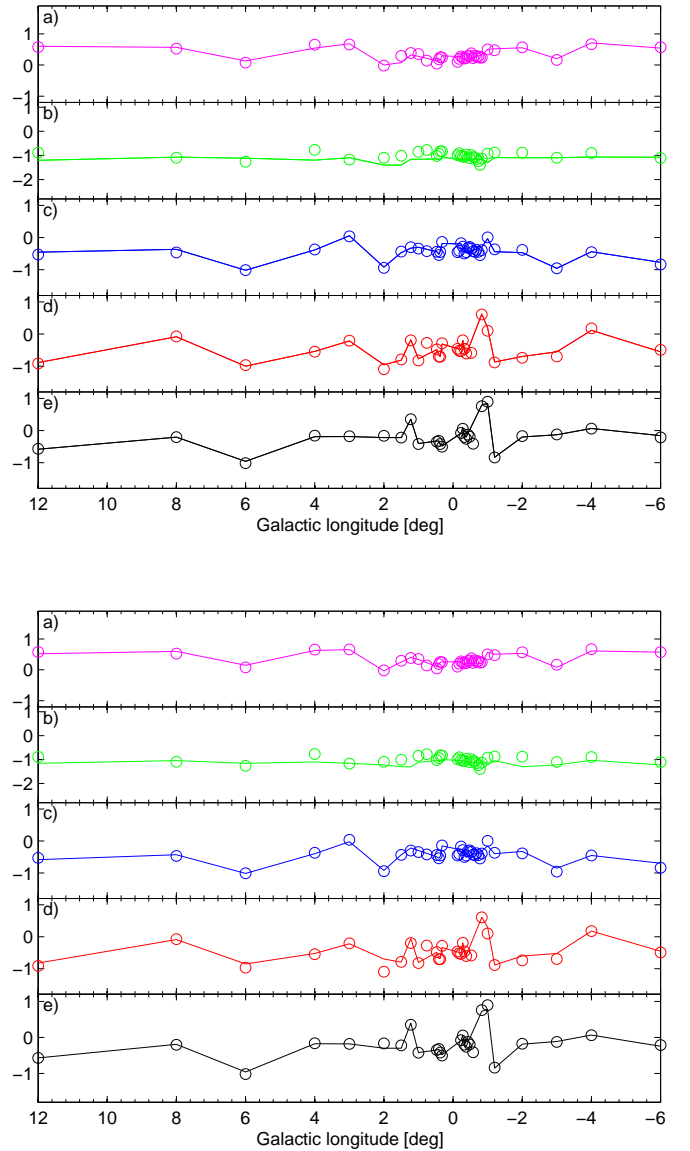


Figure 2. The observed corrected line ratios (open circles) are compared with model results (lines). Top diagrams : line ratios calculated by BB dominated models (top) and pl dominated models (bottom). Black : $\log([\text{OIII}]51.8/[\text{OI}]63.2)$; red : $\log([\text{OIII}]88.4/[\text{OI}]63.2)$; blue : $\log([\text{NII}]121.9/[\text{OI}]63.2)$; green : $\log([\text{OI}]145.5/[\text{OI}]63.2)$; magenta : $\log([\text{CII}]157.7/[\text{OI}]63.2)$.

because they are fine structure lines belonging to the same triplet. (The population of the triplet levels depends mostly on the density). The detailed modelling of the spectra leads some times to unexpected results.

Notice that the range of V_s , which gives the best fit to the data, corresponds to gas temperatures downstream near the shock front most suitable to the O^{++} ion. Throughout the region dominated by O^{++} the density trend is determined by compression which also depends on V_s .

The density affects strongly the cooling rate ($\propto n^2$), i.e. the drop of the temperature downstream which determines the III/II line ratios. In Yasuda et al. spectra, nitro-

gen and carbon appear only through a single line, [NII] and [CII], respectively. Therefore a reliable choice of the N/O and C/O relative abundances depends on the density downstream that is constrained by the oxygen line ratios.

The ionizing parameter too affects the [OIII]51.8/[OIII]81.4 line ratios as well as the III/II line ratios. Therefore V_s , n_0 , and U (F in pl models) must be calculated consistently.

Although the observed [NII]/[OI] and [CII]/[OI] line ratios can be reproduced by suitable N/O and C/O, the C/H, N/H and O/H relative abundances are not constrained by Yasuda et al spectra. A further constraint is provided by their upper limits, namely the solar abundances (e.g. Asplund et al 2009). In fact, the observed positions were purposely chosen to be the least contaminated by strong discrete sources. Moreover, dust grains and molecules which are distributed inhomogeneously throughout the ISM, trapping O, N, and C atoms, may reduce the relative abundance of these species in the gaseous phase.

3.2 Correction of the spectra

In the first modelling attempt, we obtained a satisfying fit of all the line ratios except [OI]145.5/[OI]63.2 ($\equiv R_{[OI]}$), both by a power-low flux similar to that of AGN, and by a black body spectrum.

The $R_{[OI]}$ line ratios deserve a special comment. The observed $R_{[OI]}$ were compared with the results of model calculations. $R_{[OI]}$ depends inverse-proportionally on the density. Adopting the input parameters within the ranges which give the best results for the other line ratios, the calculations give $R_{[OI]}$ close to 0.08 while the observations show ~ 0.12 . The theory (Osterbrock 1988) indicates that [OI] 145 ($^3P_0 \rightarrow ^3P_1$)/[OI] 63 ($^3P_1 \rightarrow ^3P_2$) vary between 0.06 in the high density limit and 0.19 at the low density limit. A discrepancy by a factor of ~ 1.5 (and even larger in positions at -3.0, -1.0, and 2.0 deg.) indicates that the data should be further corrected for extinction. The correction affects also the [NII] 121.9, [OI]145 and [CII] 157.7 line intensities.

We therefore calculated an appropriate value for the extinction A_V , comparing in each position the observed $R_{[OI]}$ with the value calculated at the nebula. Adopting (Rodríguez-Fernández et al. 2004) : $\tau_\lambda = \tau_{30}(30/\lambda)^\beta$ (where τ is the optical depth and $\beta = 1$ for amorphous silicate grains) A_V results ~ 47 magn, higher than 30, which is generally assumed in the GC. However, in positions -3.0, -1.0, and 2.0 deg the discrepancies between the observed $R_{[OI]}$ (0.24, 0.8, and 0.31, respectively) and the calculated ones ($\sim 0.08 - 0.01$) were still high. Correcting these single positions, we obtained $A_V = 112, 266, \text{ and } 174$ magn, respectively, in agreement with. Bally et al (2001) claim that A_V can be in excess of 100 magn.

All the lines observed in each position were corrected adopting the calculated A_V and the results are compared with a new cycle of calculations in Fig. 2. We have adopted a graphical representation of the results in order to show the profile of the line ratios throughout the observed GC region. The spectra lacking one or more lines were neglected. Fig. 2 shows that the fit of calculated to observed (corrected) line ratios is good enough for both BB and pl models.

Following our method (Paper I) we proceed by modelling the spectra from one position to the next closest one

adopting as an initial trial the conditions found in the previous one. In this way we obtain reasonable physical conditions and relative abundance with minimum fluctuations.

3.3 The physical conditions throughout the GC

The input parameters which explain the observed line ratios throughout the GC and the disc are presented in Fig. 3, except of F which appears in Fig. 1 (bottom diagram). In fact F gives some new information about the active centre in the Galaxy. In Fig. 4 some interesting results are shown. The relative abundances appear in Fig. 5. The characteristic fluctuations of the parameters in Figs. 3-5 indicate a highly inhomogeneous medium.

The radiation field

The flux F adopted as the input parameter in pl models along the GC is in units of number of photons $\text{cm}^{-2} \text{s}^{-1} eV^{-1}$ at the Lyman limit. The spectral indices are $\alpha_{UV} = -1.5$ and $\alpha_X = -0.7$.

Notice that F is relatively low ($7 < \log(F) < 10$) compared with AGN. It is similar to the fluxes characteristic of LINERs (Contini 1997) and LLAGNs (Contini 2004a). In particular, F shows a maximum near the Galactic centre between positions 1.0 and -1.0 deg., which clearly indicates an active nucleus.

Diagram (c) in the bottom panel of Fig. 4 shows the profile of the ionization parameters which were adopted to reproduce the spectra by BB (red) and pl models (blue). In the pl case U is calculated by : $U = (F/(n c (\alpha - 1))) ((E_H)^{-\alpha+1} - (E_C)^{-\alpha+1})$ (Contini & Aldrovandi 1983), where E_H is H ionization potential and E_C is the high energy cutoff, n the density, and c the speed of light.

Comparing U_{BB} (U calculated by the BB dominated models) with U_{pl} (U calculated in the pl case) Fig. 4 shows that U_{BB} is higher than U_{pl} . In fact, U_{BB} depends on the central cluster and on stars throughout the GC and in the disc. We suggest that the ionization sources in the BB case are closer to the emitting clouds than the active nucleus, therefore U_{BB} is relatively high. U_{BB} has not a specific trend on a large scale. It shows high fluctuations between 1.00 and -5.0 deg. indicating that the flux is absorbed by large dust complexes. In these regions a low star formation rate was suggested by e.g. Yasuda et al.

The ionization parameter U_{BB} and the temperature of the stars affect the spectra in the same way. We have found that T_{eff} is rather constant ($3.5-3.6 \cdot 10^4$ K) in agreement with Goicoechea et al (2004), while a weak maximum of $3.8 \cdot 10^4$ K better explain the spectra in the positions between -0.83 and -0.23 deg.

The magnetic field

We find a nearly constant magnetic field of 10^{-4} gauss (Fig. 3). Modelling the corrected data, we have considered possible deviations of B_0 . Small scale fluctuations can be generally compensated by small fluctuations of the preshock density n_0 . In fact a high transversal B_0 prevents compression downstream. The peak at position -4.0 however, seems

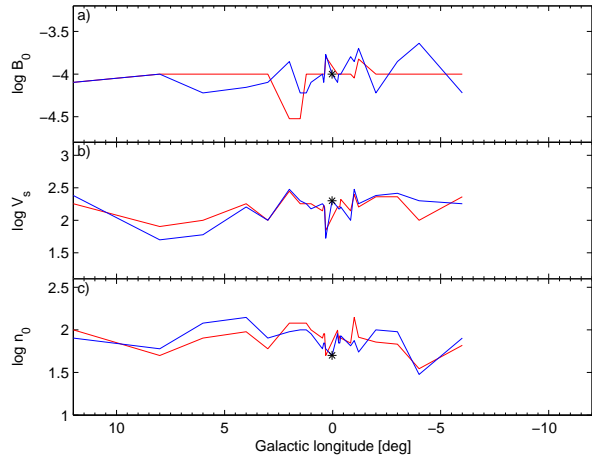


Figure 3. Comparison of BB (red) and pl (blue) models. The input physical parameters.

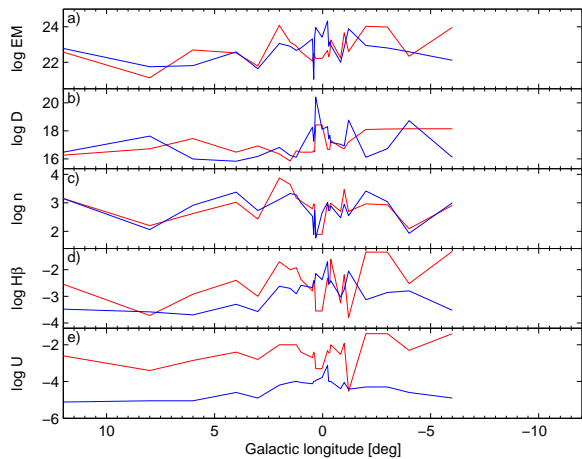


Figure 4. Comparison of BB (red) and pl (blue) models. The emission measure (EM) in $\text{cm}^{-6} \text{cm}$ (a), the geometrical thickness of the nebula (D in cm) (b), The downstream density (c), the $\text{H}\beta$ flux (in $\text{erg cm}^{-2} \text{s}^{-1}$) (d), and the ionization parameters (e) (see text).

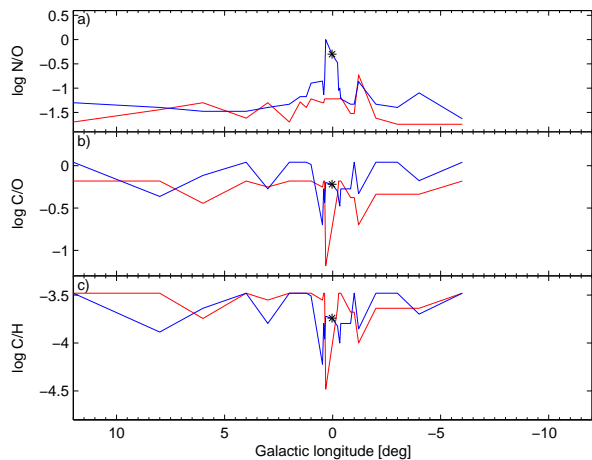


Figure 5. Comparison of BB (red) and pl (blue) models which explain the line ratios. The relative abundances.

real because the preshock density has also a minimum and the shock velocity is low.

The densities

The pre-shock density n_0 which appears in Fig. 3 represent the density in the medium upstream. Notice that BB and pl models give similar results. The gas throughout the shock-front is compressed and thermalized. Compression is determined by the adiabatic jump ($n/n_0 = 4$, where n is the density) and a further factor depends on the magnetic field and on the shock velocity. The calculations lead to densities downstream which range between ~ 100 and 2000 cm^{-3} (Fig. 4). The electron density downstream follows the recombination of the gas, which is accurately calculated throughout many slabs.

The preshock densities which lead to the best fit of the observed line ratios are $\leq 100 \text{ cm}^{-3}$, similar to those found in the regions near the GC close to the Quintuplet Cluster and the Arches Cluster but higher than those found in the ISM (Paper I). Fluctuations of n_0 in Fig. 3 show that the ISM density between the cloud fragments is $\sim 50 \text{ cm}^{-3}$. Recall, however, that the choice of the preshock density can be affected by the preshock magnetic field.

The geometrical thickness of the emitting clouds (D) and the emission measure ($\text{EM} = \Sigma n^2 D$) are also shown in Fig. 4.

The velocity field

The velocities range between a maximum of 300 km s^{-1} and a minimum of 70 km s^{-1} (BB models) and $240 - 70 \text{ km s}^{-1}$ for pl models (Fig. 3). The ranges are very similar, indicating that the shock velocity has an important role in the interpretation of the GC spectra. The fluctuations reflect an underlying turbulent regime (Paper II). The velocities are generally higher than those found near the GC ($\sim 70 \text{ km s}^{-1}$, Paper I)

Our modelling by BB models suggests that in the disc positions (-6.0, -4.0 deg) and close to the disc (-3.0 and -2.0 deg), the clouds are receding from the radiation source, while in the central region they move towards the central star cluster (and the BH).

3.4 Relative abundances

The $[\text{OIII}]51.8 / [\text{OI}]63.2$, and $[\text{OIII}]88.4 / [\text{OI}]63.2$ line ratios constrain the physical parameters (V_s , n_0 , F in pl models or U in BB models), however, nitrogen and carbon appear only throughout one line, $[\text{NII}]121.9$ and $[\text{CII}]157.7$, respectively. Our modelling determines the N/O and C/O abundance ratio in each observed position (Fig. 5), but to obtain the abundances relative to H, at least one of the C/H, N/H, and O/H, should be constrained.

The observations by Yasuda et al cover typical regions in the GC least contaminated by strong discrete sources, namely the ISM along the GC extended region. Here gas and dust are strongly coupled. We consider for instance, that C can be locked in diatomic molecules like CO, CN, CS and in carbon grains, generally in PAHs and other species (see Amo-Baladr3n et al 2011). PAH are very small grains

which are easily sputtered throughout shock fronts even for shock velocities $< 150 \text{ km s}^{-1}$. C/H (Fig. 5) is close to solar in agreement with destruction of grains by harsh radiation from the star clusters and from the AC as well as by sputtering. So we set the C/H upper limit at the solar value (Fig. 5, bottom diagram). C/H variations show in particular the distribution of dust.

A rapid comparison between Fig. 3 and Fig. 5 shows that the fluctuations in the profiles of the physical parameters are also present in the C/H, C/O, and N/O relative abundances. The C/O abundance ratio calculated by BB models is lower than solar (~ 0.5) in positions near the very centre and nearly solar in the other positions. C/O calculated by pl models is higher (≤ 1.58) than solar throughout most of the GC. Theoretically, this depends on the exponential and power-law of the radiation flux, respectively. Physically, this discrepancy shows that different conditions coexist in each of the observed position.

The calculated N/O relative abundance (~ 0.08 and ~ 0.03 in average in the pl and BB models, respectively) is lower than solar (~ 0.25) throughout most of the GC region, except in the very center. Here N/O reaches a value of ~ 1 , indicating that oxygen is strongly depleted from the gaseous phase. Unfortunately, Yasuda et al spectra do not contain Si lines, which could reveal whether dust in the GC is composed by silicate grains. C/H is rather low in the same positions indicating that CO molecules are present. The velocities are $\leq 100 \text{ km s}^{-1}$, then most of C and O can be also trapped into dust grains, while molecules such as NH_3 , NH , etc, are destroyed by radiation from the black hole.

Metallicity enhancement of CNO could derive from classical nova explosions. However, they are easily washed out by dust adsorption in the surroundings.

In order to better constrain the N/O relative abundance we select one of the spectra presented by Goicoechea et al (2004, table1) which responds to two criteria : 1) it contains data of all the observed lines including [NII] and [NIII] and 2) it is placed in the GC region ($l=0.025 \text{ deg}$, $\sim 3.5 \text{ pc}$) at a latitude $b=0 \text{ deg}$. We have corrected the spectrum for $A_V=250 \text{ mag}$ as indicated by Goicoechea et al (2004). The comparison between observed (corrected) and calculated line ratios to [OI]63.2 appears in Table 1. The model is calculated adopting $n_0=50 \text{ cm}^{-3}$, $V_s=200 \text{ km s}^{-1}$, $B_0=10^{-4} \text{ gauss}$, $F=1.3 \cdot 10^9 \text{ photons cm}^{-2} \text{ s}^{-1} \text{ eV}^{-1}$ at the Lyman limit, $C/H=1.8 \cdot 10^{-4}$, $C/O=0.6$, and $N/O=0.5$. These values are inserted in Figs. 3-5 as black asterisks. The low C/H relative to the solar value ($2.7 \cdot 10^{-4}$, Asplund et al 2009) is in agreement with the strong extinction in the very centre of the Galaxy, and with the high dust-to-gas ratios (see Sect. 4).

4 THE SED OF THE CONTINUUM

The continuum spectra presented by Yasuda et al (2008, fig. 2) cover the wavelength range $\sim 50\text{-}200 \mu\text{m}$. The models which explain the line spectra in each position are adopted to calculate consistently the free-free and free-bound emission flux from the gas and IR reprocessed radiation from dust grains. The continuum from the gas and reradiation from dust appear in Figs. 6 and 7 as two distinct curves for each model.

Table 1. comparison with Goicoechea et al (2004) spectrum

line ratios to [OI]63.2	obs.	calc.
[OIII]51.8	1.2	1.1
[NIII]57.3	0.81	0.80
[OIII]88.36	0.5	0.65
[NII]122.	0.12	0.18
[OI]145.5	0.08	0.09
[CII]157.7	0.38	0.4

4.1 Temperature of the dust grains

The grains are heated by radiation and by mutual collisions with the gas and their temperature is calculated in each of the slabs downstream at each of the observed positions. The temperature of the grains depends also on the grain radius, therefore on sputtering. Integration throughout the slabs for each model leads to the dust reprocessed radiation curve which covers a range of frequencies larger than a simple Planck function.

In Fig. 6 we compare model calculations with the LWS data of the continuum SED in two characteristic positions presented by Yasuda et al (2008, fig. 2), one in the GC and the other in the disc.

We have selected two models from the modelling of the line spectra in the GC, one at positions 0.025 deg . (from Goicoechea et al. 2004) close to the very centre, and the other at position $l=-3. \text{ deg}$, at the centre-disc limit, to model the observed data (red circles) in the GC. Both models are calculated adopting a pl flux from the active centre. The calculated maximum grain temperature is $T_{gr}=41 \text{ K}$ for the model closest to the GC and a maximum of 52 K for dust at position $l=-3 \text{ deg}$. The grain maximum temperature is proportional to the shock velocity. A grain radius $a_{gr}=1. \mu\text{m}$ is adopted.

The green circles refer to the observations from the disc. The model fitting the line spectrum at position $l=12 \text{ deg}$ reproduces the Yasuda et al data satisfactorily. The model is calculated adopting a BB photoionizing radiation flux from the stars with $T_{eff}=35000\text{K}$. The temperature of the silicate grains calculated in the slabs downstream covers the $20 - 44 \text{ K}$ temperature range.

The calculated dust temperatures are in agreement with Yasuda et al results ($14\text{-}20$ and $25\text{-}40 \text{ K}$ from source to source). However, the relatively small frequency range covered by the data does not constrain the relative intensity between the dust reradiation peak and the bremsstrahlung (see Paper I). We adopted in these models a dust-to-gas ratio of $1\text{-}5 \cdot 10^{-14}$ by number corresponding to $\sim 4 \cdot 10^{-4} - 2 \cdot 10^{-3}$ by mass for silicates.

Fig. 6 shows that the two observed curves in the FIR (Yasuda et al, fig. 2, top and bottom diagrams) can be fitted by the continuum spectra emitted from different positions. The shock velocity is the critical parameter.

We have added in Fig. 6 the black body radiation corresponding to $T_{eff}=35000 \text{ K}$ from the stars by a free Y-axis scale.

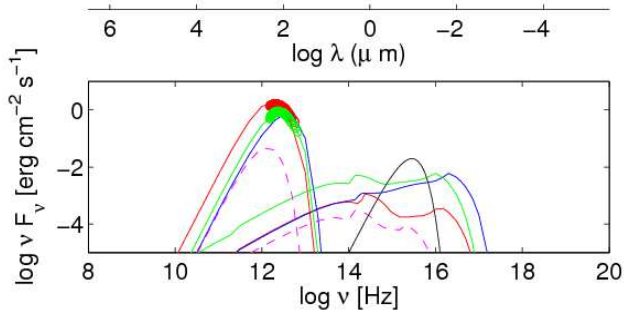


Figure 6. Comparison of calculated continuum SEDs with LWS data (Yasuda et al 2008). Red circles: the data from Yasuda et al. in the Galactic central region Green circles: the data from Yasuda et al. in the Galactic disk. Red solid lines : pl model at position $l=0.025$ deg. Blue solid lines : pl model at position $l=-3$. deg. Green lines :BB model at position $l=12$. deg. Magenta lines : BB model at position $l=8$. deg. Black line : the black body corresponding to $T_{eff}=35000$ K.

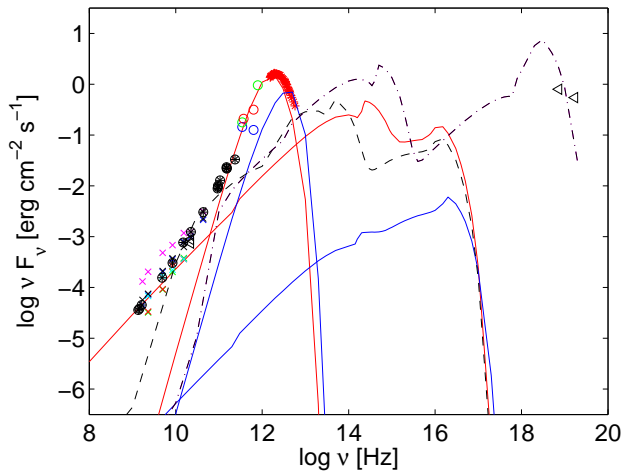


Figure 7. Comparison of calculated continuum SEDs with data. Red solid lines : pl model for position $l=0.025$ deg.; black dashed lines : pl model calculated by $n_0=3 \cdot 10^4 \text{ cm}^{-3}$ and $V_s=200 \text{ km s}^{-1}$; black dot-dashed lines : pl model calculated by $n_0=6 \cdot 10^5 \text{ cm}^{-3}$ and $V_s=3000 \text{ km s}^{-1}$; blue solid lines : pl model at position -3 deg.. Anderson et al (2004) data : black X : NGC 3147; cyan X : NGC 4579; blue X : NGC 4203; red X : NGC 4168; green X : NGC 4235; magenta X : NGC 4450. Pierce-Price et al. (2000) data in the radio : open circles. Falcke et al (1998) data : filled circles. Yasuda et al data in the IR : red asterisks. Bird et al. (2007) data for Sgr A* in the X-range : black open triangles. Petrov et al (2007) data for Sgr A* in the radio range : black open triangles

4.2 The radio-FIR range

We present in Fig. 7 the modelling of the continuum SED on a larger frequency range. We have added to the continuum SED observed in the central region (Yasuda et al 2008, fig.2, top diagram) the following data :

1) observed by SCUBA in the mm range by Pierce-Price et al (2000) (red open circles), observed by Serabyn et al (1997) with the Caltech submillimeter Observatory and JCMT (green open circles) , and observed by Zylka et al

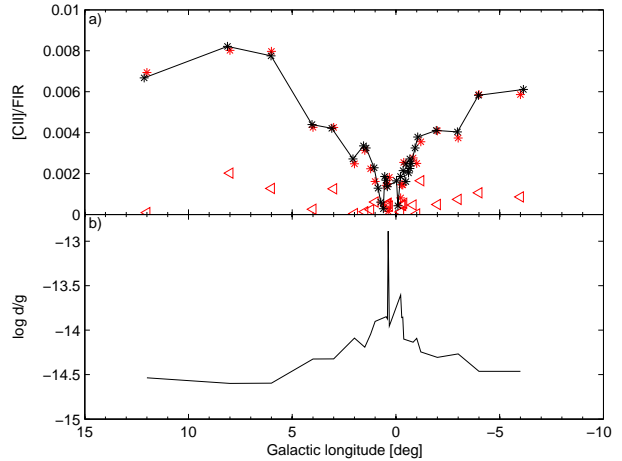


Figure 8. Top panel : comparison of model calculations (red triangles) with [CII]/FIR data (black asterisks) adapted from Yasuda et al.(2008, fig. 4) adopting [CII] and FIR values summed up from BB and pl models. Red asterisks represent the adjusted results (see text). The d/g ratios appear in the bottom panel.

(1995) (black open circles). Pierce-Price et al (2000) who investigated variability, presented data in the range between 700 and $2000 \mu\text{m}$. The data are roughly reproduced by dust FIR reradiation.

2) observations of Sgr A* corresponding to centimeter to millimeter wavelengths obtained by the VLA, the Berkeley-Illinois-Maryland Array (BIMA), the Nobayama 45 m. and the IRAM 30 m. telescope. The data were presented by Falcke et al. (1998), who explained the millimeter excess by the presence of an ultracompact component of relativistic plasma with the size of a few Schwarzschild radii near the black hole. Indeed the data cannot be reproduced by the slope of the dust reradiation curve, nor by the bremsstrahlung corresponding to the densities suitable to the observed line ratios, but they show that self-absorption of free-free radiation should be accounted for.

3) For comparison we show in Fig. 7 the SEDs of LLAGNs (NGC 3147, NGC 4579, NGC 4203, NGC 4168, NGC 4235, and NGC 4450) in the radio range presented by Anderson et al (2004, fig. 3).

During the past decade advection-dominated accretion flows have been used to explain the SED of Sgr A* and other LLAGNs (Narayan & Yi 1995; Narayan, Yi & Mahadevan 1995). Namely, a hot plasma develops in which the protons decouple from the electrons, allowing the protons to carry most of the energy released by the accretion process into the black hole, limiting the amount that is radiated away. Hot thermal electrons generate synchrotron radiation that is self-absorbed, resulting in a radio spectral index of ~ 0.4 (Mahadevan 1997). Bremsstrahlung and inverse Compton processes generate additional emission, producing a relatively well-defined spectrum from radio through X-ray frequencies (Anderson 2004).

Following our model for the GC (Papers I and II) the clouds are fragmented by the underlying turbulent regime, so many different physical conditions may coexist in different positions, in particular, close to Sgr A*. For instance, the detailed modelling of the LLAGN NGC 4579 (Contini

2004a) confirms that self-absorption of free-free radiation is crucial to reproduce the trend of the radio data.

Self-absorption requires a cloud component with densities higher than those found to reproduce the FIR spectra close to Sgr A*. The model which fits the Sgr A* radio continuum SED between 10^{10} and 10^{11} Hz is calculated by $V_s = 200 \text{ km s}^{-1}$, $n_0 = 3 \cdot 10^4 \text{ cm}^{-3}$ and $\log F = 9.1$. At lower frequencies the observations recover the trend of the bremsstrahlung emitted downstream of clouds with lower densities. At higher frequencies the data follow the dust FIR reradiation trend.

Other clouds with shock velocities up to 3000 km s^{-1} explain the X-ray data. They coexist in the very centre of the Galaxy, but are closer to the active nucleus than the low velocity gas.

4.3 Dust-to-gas ratios

We investigate the [CII]157.7/FIR ratios presented by Yasuda et al. (2008, fig. 4). First we check whether in regions close to the GC dust reprocessed radiation or bremsstrahlung dominate the FIR continuum. In Paper I we calculated the physical conditions of gas and dust in the regions photoionized by the stars near the GC and collisionally heated by shock fronts. Gas and dust are coupled collisionally and by the mutual heating and cooling of gas and dust. The grains are affected by sputtering, evaporation, etc. Shock velocities, which directly determine the frequency range of dust reprocessed radiation (Contini et al. 2004), were constrained by the FWHM of line profiles in the observed spectra. By modelling the SED of the continuum it was found that indeed dust reradiation dominates the FIR.

We will refer to [CII]/FIR, neglecting the [OI]63.2/FIR ratio, because [CII]/[OI] is rather constant (Fig. 2, diagrams a)) and almost always > 1 . Anyway, Fig. 6 shows that both the FIR lines appear in the range dominated by dust reradiation. We present Yasuda et al ISO data (black asterisks) in Fig. 8 (top panel) as well as model results (red open triangles).

The [CII] lines and the integrated FIR continua were obtained by summing up the results of BB and pl models, adopting the same relative weights for the two models. The calculations were repeated in all the observed positions. Recall that the FIR continuum is highly dominated by dust reprocessed radiation, while the [CII] lines are emitted by the gas. The temperature of the grains and the line intensities emitted by the gas are calculated consistently in each slab downstream.

The dust-to-gas ratio determines directly the relative intensity of the dust reradiation peak to the bremsstrahlung. Changing the d/g parameter by a factor ≤ 100 in a model would affect the line ratios by very small factors ($< 1\%$), while large d/g alterations can lead to a drastic different situation in shock dominated regimes, e.g. from a non radiative to a radiative shock (Contini 2004b).

Fig. 8 shows that, even if the trend of the models reproduces qualitatively the data, the fit is not satisfying. Recall that the FIR fluxes are $\propto d/g$ and that the models were calculated adopting $d/g = 10^{-14}$ by number ($\sim 4 \cdot 10^{-4}$ by mass). Therefore to increase the [CII]/FIR ratios, the calculated FIR fluxes should be divided by an adjusting factor $f_{d/g}$ in each position. The [CII]/FIR calculated ratios best

fitting the data (red asterisks) were re-calculated adopting $d/g = 10^{-14} / f_{d/g}$. The results are presented graphically in the bottom panel of Fig. 8. The profile of d/g throughout the GC shows that there is an accumulation of dust in the very centre.

Yasuda et al (2008, fig. 4) discuss the [CII] /FIR minimum between -1 and 0 deg. on the basis of the FUV radiation, a spectrally soft radiation flux, and high gas densities. All these parameters are accounted for by our models and lead to consistent results.

5 DISCUSSION AND CONCLUDING REMARKS

Goicoechea et al (2004) claim that the coupled effect of collisional and radiative-type heating mechanisms *seem the rule in Sgr B2 and in the bulk of GC molecular clouds* observed by ISO (Rodríguez-Fernandez et al 2004). Cloud complexes near $l = 1.3, 3$ and 5 deg have velocities of $100\text{-}200 \text{ km s}^{-1}$ in regions less than 0.5 deg (~ 75 pc) in diameter (Dame et al. 2001); Listz 2006, 2008). Bally et al. (2010) notice that the cloud complexes may trace the locations where gas is entering the dust lanes at the leading edges of the bar in the center of the Galaxy passing through a series of shocks (Listz 2006), or dust lanes along the bar's leading edge which is seen nearly end-on.

A complex network of filaments created by fragmentation at the shock fronts was found near the GC by modelling the near-IR spectra in Papers I and II.

However, low velocity shocks (Hüttemeister et al 1995, Martín-Pintado et al 1997) are not the only heating mechanism, because a dense stellar population in the central cluster and throughout the GC heats and ionizes gas and dust.

The modelling of the FIR spectra observed by Yasuda et al (2008) throughout the very centre of the Galaxy and in some disc positions, shows that the physical conditions and the relative abundances fluctuate within reasonable limits. For instance, the velocities range between 50 and 300 km s^{-1} , the gas preshock densities within 30 and 100 cm^{-3} , and the ionization parameters (referring to the BB flux from the stars) range between $2 \cdot 10^{-4}$ and $2 \cdot 10^{-2}$.

The calculation of the FIR spectra adopting a power-law flux, characteristic of AGN, leads to interesting results. First, the LLAGN character of the Galaxy is confirmed by a pl maximum radiation of $F \sim 6 \cdot 10^9 \text{ photons cm}^{-2} \text{ s}^{-1} \text{ eV}^{-1}$ close to the Sgr A* position (Fig. 1, bottom diagram). The maximum F flux is very similar to that found by consistent modelling of NGC 4579 ($\leq 10^{10}$ Contini 2004a) and at least by a factor of 100 lower than in AGNs.

Fig. 4 shows that the corresponding ionization parameter U_{pl} decreases with distance from the centre, while the ionization parameter (U_{BB}) calculated by BB dominated models has no specific trend, but a fluctuating profile. U_{BB} is due to radiation from the stars, adopting that a temperature $T_{eff} \sim 36000 \text{ K}$ permeates the inhomogeneous medium in the GC. Moreover, U_{pl} is lower by a factor of ~ 100 than U_{BB} . This result suggests that in the observed positions, the stars should be located closer to the emitting gaseous clouds than the active nucleus. However, Yasuda et al observations refer to regions *least contaminated by strong discrete sources*. This strengthens the AGN presence in the GC.

Even if the AGN in the Galaxy is weak and the lines in the UV-optical range are invisible, we have calculated the $H\beta$ absolute flux throughout the GC by both BB and pl models. Fig. 4 shows that, in a small region between about -0.2 and 0.2 deg, the $H\beta$ flux would trace the LLAGN rather than the central star cluster.

Reprocessed radiation from the dust which is coupled to the gas throughout the shock front peaks at $\sim 100 \mu\text{m}$. The FIR SED of the continuum flux from the very centre is different from that emitted from the positions near the disc, because it depends on the physical conditions of the gas, in particular on the shock velocity.

The dust-to-gas ratios calculated in the GC are $10^{-15} \leq d/g \leq 10^{-13}$, never reaching, however, the values characteristic of IR luminous galaxies (Contini & Contini 2007) even close to the centre. The d/g were derived from the fit of the observed $[\text{CII}]/\text{FIR}$ ratios.

The modelling of the continuum near the Sgr A* position shows that the radio SED results from the contribution of clouds with different densities and velocities. A pre-shock density $n_0 \sim 3 \cdot 10^4 \text{ cm}^{-3}$ combined with $V_s = 200 \text{ km s}^{-1}$ leads to densities downstream $\sim 5 \cdot 10^6 \text{ cm}^{-3}$, high enough for self-absorption of free-free radiation in the radio range. Such high densities were observed in the circumnuclear disc (Amo-Baladrón et al. 2011). At low frequencies ($< 10^{10} \text{ Hz}$) the observations recover the trend of the bremsstrahlung emitted downstream of clouds with lower densities.

The radio flux is variable on scales of weeks to months. While synchrotron self-Compton is an important component, thermal bremsstrahlung from the accretion flow plays an important role (Falcke, H. & Markoff, S. 2000). The variability in the EUV to X-ray band is correlated to variability in the sub-mm. The scale of weeks and months could be explained by the high fragmentation of the medium crossed by the shock front.

High velocity components are revealed by the X-ray data (Bird et al 2007). Observations from the Sgr A* source are explained by high-velocity shocks ($V_s \sim 3000 \text{ km s}^{-1}$) characteristic of jets. This velocity corresponds to a post-shock temperature of $\sim 10^8 \text{ K}$. The observation of the 6.7 keV helium like Fe line (Sunyaev et al. 1993) argues for thermal bremsstrahlung as a possible emission mechanism. However, the age of the source cannot be more than $\sim 3 \cdot 10^4$ years (Chevalier 1982, adopting a radius of $\sim 400 \text{ pc}$) if there is not a continuous heating mechanism.

The high velocity could be the shock velocity accompanying the blast wave from a supernova outburst. In fact the X-ray flux is variable and decaying. However, the hypothesis of a supernova origin in the GC is excluded by Koyama et al (1996) because there is no indication of repeated supernova outbursts.

REFERENCES

- Aitken, D.K. et al. 2000, *Apl*, 534, L173
 Amo-Baladrón, M.A., Martín-Pintado, J., Martín, S. 2011, *A&A*, 526, A54
 Anderson, J.M., Ulvestad, J.S., Ho, L.C. 2004, *ApJ*, 603, 42
 Asplund, M., Grevesse, N., Sauval, A.J., Scott, P. 2009, *ARA&A*, 47, 481
 Bally, J.; Stark, A. A.; Wilson, R. W.; Henkel, C. 1988, *ApJ*, 324, 223
 Bally, J. et al. 2010, *ApJ*, 721, 137
 Bird, A.J. et al. 2007, *ApJS*, 170, 175
 Chevalier, R.A. 1982, *ApJ*, 259, L85
 Contini, M. 1997, *A&A*, 323, 71
 Contini, M. 2004a, *MNRAS*, 354, 675
 Contini, M. 2004b, *A&A*, 422, 591
 Contini, M. 2009 *MNRAS*, 399, 1175, Paper I
 Contini, M., Aldrovandi, S.M.V. 1983, *A&A*, 127, 15
 Contini, M., Contini, T. 2007, *AN*, 328, 953
 Contini, M., Goldman, I. 2010, *MNRAS.tmp.1752*, Paper II
 Contini, M., Viegas, S.M., Campos, P.E. 2003, *MNRAS*, 346, 37
 Contini, M., Viegas, S. M., Prieto, M. A. 2002 *A&A*, 386, 399
 Contini, M., Viegas, S. M., Prieto, M. A. 2004, *MNRAS*, 348, 1065
 Contini, M., Radovich, M., Rafanelli, P., Richter, G.M. 2002, *ApJ*, 572, 124
 Cotera, A.S.; Erickson, E.F.; Colgan, S.W.J.; Simpson, J.P.; Allen, D.A.; Burton, M.G. 1996, *ApJ*, 461, 750
 Cotera, A. S., Colgan, S. W. J., Rubin, R. H., Simpson, J. P. 2005, *ApJ*, 622, 333
 Dame, T. M.; Hartmann, D.; Thaddeus, P. 2001, *ApJ*, 547, 792
 Eisenhauer, G. et al. 2005, *ApJ*, 628, 246
 Falcke, H., Goss, W.M., Matsuo, H., Teuben, P., Zhao, J-H., Zylka, R. 1998, *ApJ*, 499, 731
 Falcke, H. Markoff, S. 2000, *A&A*, 362, 113
 Genzel, R., Eisenhauer, F., Gillessen, S. 2010, *Rev. Mod. Phys.*, 82, 3121
 Ghez, A.M. et al. 2003, *ApJ*, 586, L127
 Ghez, A.M. et al. 2005, *ApJ*, 620, 744
 Goicoechea, J.R., Rodriguez-Fernandez, N.J., Cernicharo, J. 2004, *ApJ*, 600, 214
 Hüttemeister, S., Wilson, T. L., Mauersberger, R., Lemme, C., Dahmen, G., Henkel, C. 1995, *A&A*, 294, 667
 Koyama, K.; Maeda, Y.; Sonobe, T.; Takeshima, T.; Tanaka, Y.; Yamauchi, S., 1996, *PASJ*, 48, 249
 Lis, D. C.; Serabyn, E.; Zylka, R.; Li, Y. 2001, *ApJ*, 550, 761
 Liszt, H. S. 2006, *A&A*, 447, 533
 Liszt, H. S. 2008, *A&A*, 486, 467
 Mahadevan, R. 1997, *ApJ*, 477, 585
 Martín-Pintado, J., de Vicente, P., Fuente, A., Planesas, P. 1997, *ApJ*, 482, L45
 McKee, C.F., Tan, J.C. 2003, *ApJ*, 585, 850
 Morris, M.; Yusef-Zadeh, F. 1989, *ApJ*, 343, 703
 Nagata, T., Woodward, C.E., Shure, M., Kobayashi, N. 1995, *AJ*, 109, 1676
 Narayan, R., Yi, I. 1995, *ApJ* 444, 231
 Narayan, R., Yi, I., Mahadevan, R. 1995, *Natur*, 374, 623
 Osterbrock, D.E. 1988 in 'Astrophysics of gaseous nebulae and active galactic nuclei', University Science Books
 Petrov, L., Hirota, T., Honma, M., Shibata, K. M., Jike, T., Kobayashi, H. 2007, *AJ*, 133, 2487
 Pierce-Price, J. S. et al. 2000, *ApJ*, 545, L121
 Rodríguez-Fernández, N. J.; Martín-Pintado, J.; Fuente, A.; Wilson, T. L. 2004, *A&A*, 427, 217
 Schödel, R., Bower, G.C., Muno, M.P., Nayakshin, S., Ott, T. 2006, *Journal of Physics: Conference Series*, Volume 54, Proceedings of "The Universe Under the Micro-

- scope - Astrophysics at High Angular Resolution”, held 21-25 April 2008, in Bad Honnef, Germany. Editors: Rainer Schoedel, Andreas Eckart, Susanne Pfalzner and Eduardo Ros, pp. (2006).
- Schödel, R. et al. 2003, AN, 324, 535
- Serabyn, E., Carlstrom, J., Lay, O., Lis, D. C., Hunter, T. R., Lacy, J. H. 1997, ApJ, 490, L77
- Simpson, J P.; Colgan, S. W. J., Cotera, A. S., Erickson, E. F., Hollenbach, D. J., Kaufman, M. J., Rubin, R. H. 2007, ApJ, 670, 1115
- Sunyaev, R.A., Markewitch, M., Pavlinsky, M. 1993, ApJ, 407, 606
- Spergel, D. N.; Blitz, L. 1992 Natur., 357, 665
- Yasuda, A., Nakagawa, T., Spaans, M., Okada, Y., Kaneda, H. 2008, A&A, 480, 157
- Zylka, R., Mezger, P. G., Ward-Thompson, D., Duschl, W. J., Lesch, H. 1995, A&A, 297, 83